

# Hyperspectral Image Target Detection Improvement Based on Total Variation

Shuo Yang and Zhenwei Shi, *Member, IEEE*

## Abstract

For the hyperspectral target detection, the neighbors of a target pixel are very likely to be target pixels, and those of a background pixel are very likely to be background pixels. In order to utilize this spatial homogeneity or smoothness, based on total variation (TV), we propose a novel supervised target detection algorithm which uses a single target spectrum as the prior knowledge. TV can make the image smooth, and has been widely used in image denoising and restoration. The proposed algorithm uses TV to keep the spatial homogeneity or smoothness of the detection output. Meanwhile, a constraint is used to guarantee the spectral signature of the target unsuppressed. The final formulated detection model is an  $\ell_1$  norm convex optimization problem. The Split Bregman algorithm is used to solve our optimization problem, as it can solve the  $\ell_1$  norm optimization problem efficiently. Two synthetic and two real hyperspectral images are used to do experiments. The experiment results demonstrate that the proposed algorithm outperforms other algorithms for the experiment data sets. The experiment results also show that even when the target occupies only one pixel, the proposed algorithm can still obtain good results. This is because in such case, the background is kept smooth, but at the same time the algorithm allows for sharp edges in the detection output.

## Index Terms

Hyperspectral image, target detection, total variation, Split Bregman algorithm.

## I. INTRODUCTION

Hyperspectral image target detection is a research focus in the remote sensing image processing field, because of its wide applications both in military and civil fields. The hyperspectral image, with two spatial dimensions and one spectral dimension, is a kind of 3-D data [1]. In the hyperspectral image, each pixel has a nearly continuous

The work was supported by the National Natural Science Foundation of China under Grant 61273245; by the Beijing Natural Science Foundation under Grant 4152031; by the funding project of State Key Laboratory of Virtual Reality Technology and Systems, Beihang University, under Grant VR-2014-ZZ-02; and by the Fundamental Research Funds for the Central Universities under Grant YWF-14-YHXY-028 and YWF-15-YHXY-003.

S. Yang (e-mail: shuoyangbuaa@gmail.com) and Z. Shi (Corresponding Author, e-mail: shizhenwei@buaa.edu.cn) are with State Key Laboratory of Virtual Reality Technology and Systems, School of Astronautics, Beihang University, Beijing 100191, China and with Beijing Key Laboratory of Digital Media, Beihang University, Beijing 100191, China and also with Image Processing Center, School of Astronautics, Beihang University, Beijing 100191, China.

spectrum with hundreds of very narrow bands (the width of each band is usually about 10 nm), and the same spectral band of every pixel can form a 2-D image [1], [2], [3].

In past decades, several hyperspectral image target detection algorithms have been developed. Spectral angle mapper (SAM) [4] is a very simple detection algorithm which measures the spectral angle between the spectrum of the test pixel and the prior spectral signature of target. Constrained energy minimization (CEM) [5], [6] is a finite impulse response filter minimizing the total output energy subject to a constraint that the output of the spectral signature of target is 1. The formulation of another famous detection algorithm matched filter (MF) [1] is very similar to that of CEM. In fact, if the mean of the hyperspectral data is removed before the detection process, the MF equals the CEM [1]. However, MF derives from binary hypothesis testing, which is different from CEM. Another two detection algorithms, adaptive coherence/cosine estimator (ACE) [1], [7], [8], [9] and adaptive matched filter (AMF) [1], [10], [11] are also based on hypothesis testing.

Orthogonal subspace projection (OSP) [12] and adaptive subspace detector (ASD) [2], [13], [14] are two representative subspace based target detection algorithms. OSP first projects the spectrum of the test pixel onto the orthogonal subspace of background signatures, and then finds a vector operator maximizing the residual target signature signal-to-noise ratio (SNR). ASD derives from a binary hypothesis testing problem. OSP and ASD not only require the prior knowledge of the spectral signature of target, but also the prior knowledge of spectral signatures of background which is hard to obtain in many cases [15].

Some sparse representation based target detection algorithms [16], [17], [18] have been proposed in recent years. These algorithms first build an overcomplete spectral dictionary which usually contains hundreds of spectra including both target spectra and background spectra. Then the spectrum of each pixel in the hyperspectral image is assumed to be a linear combination of only a few spectra contained in the spectral dictionary. Thus, the target detection problems can be transformed to sparse recovery problems which can be represented by  $\ell_0$  norm optimization problems. It is hard to solve the  $\ell_0$  norm optimization problem [19]. In [16], [17], [18], the  $\ell_0$  norm optimization problems are all solved by greedy algorithms. Greedy algorithms cannot guarantee to find optimal solutions, and whether greedy algorithms can find optimal solutions or not depends on the used spectral dictionary [20]. In addition, for sparse representation based detection algorithms, the choice of the spectral dictionary will also affect final detection results. Some other hyperspectral target detection algorithms have also been proposed, such as the kernel based detection algorithms [21], [22], the manifold learning based detection algorithm [23] and the metric learning based detection algorithms [24], [25].

For the hyperspectral image target detection, including spatial information can improve the detection result. Total variation (TV) [26], [27], [28], [29] can constrain the spatial homogeneity of neighboring pixels [29]. In this paper, based on TV, we propose a supervised hyperspectral image target detection algorithm which uses a single target spectrum as the prior knowledge. The proposed total variation based hyperspectral target detection (TVHTD) algorithm utilizes TV to take advantage of the spatial information of the hyperspectral image. In image processing field, TV has been used in image denoising and restoration [26], [30], and has obtained good results. Using TV for image denoising and restoration can make images smooth and keep sharp edges [26], [30]. In [29], TV is used

as a regularizer for sparse hyperspectral unmixing to constrain that for the same endmember, neighboring pixels have similar fractional abundances. In this paper, for hyperspectral image target detection, we do not use TV as a regularizer but directly use TV to construct the objective function. Unlike the sparse hyperspectral unmixing method proposed in [29], our algorithm does not need a spectral dictionary. For the hyperspectral image target detection, the neighbors of a target pixel are very likely to be target pixels, and those of a background pixel are very likely to be background pixels. We use TV to constrain this spatial homogeneity or smoothness. We find an optimal projection vector which minimizes the TV of the output under a constraint that the output of the target spectral signature is 1. The constraint used in the proposed algorithm can guarantee the target spectra unsuppressed in the output. The proposed detection model can be formulated as an  $\ell_1$  norm convex optimization problem. For the  $\ell_1$  norm optimization problem, the Split Bregman algorithm [31] is very efficient in convergence speed [31]. Thus in this paper, the Split Bregman algorithm is used to solve our detection model.

The rest of this paper is organized as follows. In Section II, we propose our novel detection model. The Split Bregman algorithm is applied to solve the proposed detection model in Section III. Some experiment results and discussions are given in Section IV. Finally, Section V gives the conclusion.

## II. DETECTION MODEL

Suppose a hyperspectral image has  $M$  columns and  $N$  rows with  $L$  bands. Let  $\mathbf{x}_0(i, j) \in \mathbb{R}^L$  ( $i = 1, \dots, M$ ,  $j = 1, \dots, N$ ) denote the spectrum of the pixel locating at column  $i$  and row  $j$ , and let  $\mathbf{s}_0 \in \mathbb{R}^L$  denote the spectral signature of target that is to be searched for in the hyperspectral image.  $\mathbf{s}_0$  can be obtained from the spectral library as a prior knowledge. For the real hyperspectral image target detection, the prior knowledge of target is hard to obtain. So in this paper, like the classical detection algorithms CEM, AMF, SAM and so on, we only use a single spectrum of target, i.e.,  $\mathbf{s}_0$ , as the prior knowledge of target. Let  $\mathbf{x}$  and  $\mathbf{s}$  be the mean removed spectrum of a pixel and the mean removed spectral signature of target, respectively. That is  $\mathbf{s} = \mathbf{s}_0 - \boldsymbol{\mu}$  and  $\mathbf{x} = \mathbf{x}_0 - \boldsymbol{\mu}$  where  $\boldsymbol{\mu}$  is the mean of the hyperspectral image. In our proposed algorithm, we use  $\mathbf{x}$  and  $\mathbf{s}$ .

The spectrum of a pixel  $\mathbf{x}(i, j)$  is an  $L$  dimensional vector, and the detection result of  $\mathbf{x}(i, j)$  should be a scalar value which indicates how likely the pixel contains the target. One effective method is to find a projection vector  $\mathbf{w} \in \mathbb{R}^L$  and use  $\mathbf{w}^T \mathbf{x}(i, j)$  as the detection output. In the projection space, the projections of target pixels should have large values and those of background pixels should have small values, so that the target and the background can be separated. The idea of projecting the spectrum of a pixel to a projection vector has been used in CEM, and has also been used in [32], where the authors proposed an algorithm for hyperspectral image spatial multiple materials detection. The idea of using  $\mathbf{w}^T \mathbf{x}(i, j)$  can be seen as an approach of projection pursuit [33], [34]. In [33], projection pursuit is used for unsupervised hyperspectral image analysis, and in [34], projection pursuit is used for unsupervised hyperspectral image target detection.

In this paper, we develop a total variation based hyperspectral target detection (TVHTD) algorithm. For TVHTD, the output detection result of  $\mathbf{x}(i, j)$  is  $\mathbf{w}^T \mathbf{x}(i, j)$ . The output detection result of every pixel can form an image  $u$ , where  $u(i, j) = \mathbf{w}^T \mathbf{x}(i, j)$ . The total variation of  $u$  can describe the piecewise spatial smoothness or homogeneity

of  $u$  [29]. Since the neighboring pixels of a target pixel are very likely to be target pixels and those of a background pixel are very likely to be background pixels, minimizing the total variation of  $u$  can keep this spatial smoothness or homogeneity property of the detection output  $u$ .

If there is no constraint, we can find that  $\mathbf{w} = \mathbf{0}$  is the optimal solution. Because in such case, all elements of  $u$  equal 0, and  $u$  has the minimal total variation value equaling 0. Obviously, in such case the detection fails. We use a constraint  $\mathbf{w}^T \mathbf{s} = 1$  to guarantee that the target pixels have large output values while suppressing the outputs of background pixels. The constraint is the same as that in CEM, except that CEM uses the constraint  $\mathbf{w}^T \mathbf{s}_0 = 1$ . Let  $\mathbf{x}_b$  denote the spectrum of the background pixel and  $\mathbf{x}_s$  denote the spectrum of the target pixel. We hope the output of the background pixel  $\mathbf{w}^T \mathbf{x}_b$  be small and the output of the target pixel  $\mathbf{w}^T \mathbf{x}_s$  be large. Similar to CEM, minimizing the total variation of  $u$  can suppress the output values. If we add a constraint  $\mathbf{w}^T \mathbf{s} = c$  where  $c$  denotes a constant, the output of the target pixel  $\mathbf{w}^T \mathbf{x}_s$  will not be suppressed. Since minimizing the total variation of  $u$  can suppress output values of pixels, the output of the background pixel  $\mathbf{w}^T \mathbf{x}_b$  has to be suppressed. In this way, the target and the background can be separated in the detection output  $u$ . The value of  $c$  does not affect the direction of optimal  $\mathbf{w}$  and thus does not affect the final detection result. In this paper, we use the constraint  $\mathbf{w}^T \mathbf{s} = 1$ . In addition, the constraint  $\mathbf{w}^T \mathbf{s} = 1$  will make target pixels and background pixels have different outputs, so minimizing the total variation of  $u$  will not make the outputs have spatial homogeneity among target pixels and background pixels.

Now, we can give the detection model of the TVHTD algorithm:

$$\begin{aligned} \mathbf{w} &= \arg \min_{\mathbf{w}} |u|_{TV} \\ \text{s.t. } &\mathbf{w}^T \mathbf{s} = 1, \end{aligned} \quad (1)$$

where  $|u|_{TV}$  denotes the total variation of  $u$ . Here we use the nonisotropic total variation [31]:  $|u|_{TV} = |\nabla_x u|_1 + |\nabla_y u|_1$ , where  $|\cdot|_1$  denotes the  $\ell_1$ -norm;  $\nabla_x u$  and  $\nabla_y u$  are the gradients of  $u$  in the horizontal direction and vertical direction, respectively.

We define two matrices  $\mathbf{H} \in \mathbb{R}^{L \times MN}$  and  $\mathbf{V} \in \mathbb{R}^{L \times MN}$ , whose columns are the finite horizontal and vertical difference of  $\mathbf{x}(i, j)$ , respectively. We have  $|\mathbf{H}^T \mathbf{w}|_1 = \sum_{i=1}^M \sum_{j=1}^N |\mathbf{w}^T \mathbf{x}(i, j) - \mathbf{w}^T \mathbf{x}(i-1, j)|$  and  $|\mathbf{V}^T \mathbf{w}|_1 = \sum_{i=1}^M \sum_{j=1}^N |\mathbf{w}^T \mathbf{x}(i, j) - \mathbf{w}^T \mathbf{x}(i, j-1)|$ . So (1) is equal to

$$\begin{aligned} \mathbf{w} &= \arg \min_{\mathbf{w}} |u|_{TV} \\ &= \arg \min_{\mathbf{w}} \sum_{i=1}^M \sum_{j=1}^N |\mathbf{w}^T \mathbf{x}(i, j) - \mathbf{w}^T \mathbf{x}(i-1, j)| \\ &\quad + \sum_{i=1}^M \sum_{j=1}^N |\mathbf{w}^T \mathbf{x}(i, j) - \mathbf{w}^T \mathbf{x}(i, j-1)| \\ &= \arg \min_{\mathbf{w}} |\mathbf{H}^T \mathbf{w}|_1 + |\mathbf{V}^T \mathbf{w}|_1 \\ \text{s.t. } &\mathbf{s}^T \mathbf{w} = 1. \end{aligned} \quad (2)$$

We assume the image is periodic, so we use  $|\mathbf{w}^T \mathbf{x}(1, j) - \mathbf{w}^T \mathbf{x}(M, j)|$  to compute  $|\mathbf{w}^T \mathbf{x}(1, j) - \mathbf{w}^T \mathbf{x}(0, j)|$  and

use  $|\mathbf{w}^T \mathbf{x}(i, 1) - \mathbf{w}^T \mathbf{x}(i, N)|$  to compute  $|\mathbf{w}^T \mathbf{x}(i, 1) - \mathbf{w}^T \mathbf{x}(i, 0)|$ . Although (2) is a convex optimization problem, it is hard to solve because of the non-smoothness of the  $\ell_1$ -norm. In the following section we will apply the Split Bregman method [31] to solve (2) efficiently. Suppose the solution to (2) is  $\mathbf{w}^*$ , then we can get the detection output of the pixel  $\mathbf{x}(i, j)$ :  $y(i, j) = \mathbf{w}^{*T} \mathbf{x}(i, j)$ . Further, to determine whether the target is present in a pixel or not, a threshold  $\eta$  can be set. If  $y(i, j) > \eta$ , the target is determined to be present in the pixel  $(i, j)$ ; else the target is determined to be absent in this pixel. The larger  $\eta$  is set to, the more pixels are determined to target present pixels. A large  $\eta$  will lead to a high probability of detection and also a high false alarm rate, and vice-versa.

### III. APPLY THE SPLIT BREGMAN METHOD TO SOLVE THE DETECTION MODEL

The Split Bregman method which can solve the  $\ell_1$  regularized problems efficiently was first proposed in [31]. The Split Bregman method is based on Bregman iteration [35], which was first used in image processing by Osher et al. in [30]. In this section, with reference to [30], [31], we apply the Split Bregman method to solve our detection model (2). We give the Split Bregman iteration procedure for our detection model in Algorithm 1. For more details about the Split Bregman method, readers could see [30], [31] for reference.

In Algorithm 1,  $(d_x^{k+1})_p$ ,  $(d_y^{k+1})_p$ ,  $(b_x^k)_p$  and  $(b_y^k)_p$  are the  $p$ th elements of  $\mathbf{d}_x^{k+1}$ ,  $\mathbf{d}_y^{k+1}$ ,  $\mathbf{b}_x^k$  and  $\mathbf{b}_y^k$ , respectively.  $shrink(\cdot)$  is the shrinkage function defined below [31]:

$$shrink(x, \gamma) = \begin{cases} \frac{x}{|x|} * \max(|x| - \gamma, 0) & x \neq 0; \\ 0 & x = 0. \end{cases} \quad (3)$$

Through experiments, we find that  $\lambda = 2$ ,  $\beta = 10^5$ ,  $\varepsilon = 10^{-6}$  and  $T = 3$  could get satisfactory results. So in the experiments of this paper, we set  $\lambda = 2$ ,  $\beta = 10^5$ ,  $\varepsilon = 10^{-6}$  and  $T = 3$ .

---

**Algorithm 1** Split Bregman iteration procedure for TVHTD
 

---

**Input:**

1. Hyperspectral image data  $\mathbf{x}(i, j) \in \mathbb{R}^L$  ( $i = 1, \dots, M, j = 1, \dots, N$ ) and the spectral signature of the target  $\mathbf{s} \in \mathbb{R}^L$ . Suppose the mean of the hyperspectral image has been removed from  $\mathbf{x}(i, j)$  and  $\mathbf{s}$ .

**Initialization:**

2. Set  $k = 0$ ,  $\mathbf{w}^0 = \mathbf{0}$ ,  $\mathbf{d}_x^0 = \mathbf{0}$ ,  $\mathbf{d}_y^0 = \mathbf{0}$ ,  $\mathbf{b}_x^0 = \mathbf{0}$ ,  $\mathbf{b}_y^0 = \mathbf{0}$  and  $f^0 = 0$ . Set  $\lambda > 0$ ,  $\beta > 0$  and a tolerance  $\varepsilon > 0$ .

**Iteration:**

3. For  $l = 1$  to  $T$

$$4. \quad \mathbf{w}^{k+1} = (\beta \mathbf{s} \mathbf{s}^T + \lambda \mathbf{H} \mathbf{H}^T + \lambda \mathbf{V} \mathbf{V}^T)^{-1} (\beta f^k \mathbf{s} + \lambda \mathbf{H} \mathbf{d}_x^k - \lambda \mathbf{H} \mathbf{b}_x^k + \lambda \mathbf{V} \mathbf{d}_y^k - \lambda \mathbf{V} \mathbf{b}_y^k).$$

$$5. \quad (d_x^{k+1})_p = \mathit{shrink}((\mathbf{H}^T \mathbf{w}^{k+1})_p + (b_x^k)_p, \frac{1}{\lambda}).$$

$$6. \quad (d_y^{k+1})_p = \mathit{shrink}((\mathbf{V}^T \mathbf{w}^{k+1})_p + (b_y^k)_p, \frac{1}{\lambda}).$$

$$7. \quad \mathbf{b}_x^{k+1} = \mathbf{b}_x^k + \mathbf{H}^T \mathbf{w}^{k+1} - \mathbf{d}_x^{k+1}.$$

$$8. \quad \mathbf{b}_y^{k+1} = \mathbf{b}_y^k + \mathbf{V}^T \mathbf{w}^{k+1} - \mathbf{d}_y^{k+1}.$$

9. end

$$10. \quad f^{k+1} = f^k + 1 - \mathbf{s}^T \mathbf{w}^{k+1}.$$

11.  $k \leftarrow k + 1$ .

**Stop criterion:**

12. If  $|\mathbf{s}^T \mathbf{w} - 1| < \varepsilon$ , go to step 13; else go back to step 3.

**Output:**

13. The final detection output:  $y(i, j) = \mathbf{w}^T \mathbf{x}(i, j)$ .

---

The Split Bregman iteration is a classical and famous algorithm, which belongs to the class of proximal methods [38]. Several convergence analyses have been given by researchers. So we do not give convergence analyses in this paper. The reader could see [30], [31], [36], [37], [38] and references therein for convergence analyses.

#### IV. EXPERIMENT RESULTS AND DISCUSSION

In this section, we use two synthetic hyperspectral images and two real hyperspectral images to do experiments. Two real hyperspectral images are collected by airborne visible/infrared imaging spectrometer (AVIRIS) and hyperspectral mapper (HyMap), respectively. The compared algorithms include CEM [5], ACE [1], AMF [1], SAM [4] and the sparse representation algorithm proposed in [16]. The sparse representation algorithm is designed for finding multiple pixel targets. The outputs of CEM [5], ACE [1], AMF [1] and SAM [4] are given below:

$$D_{CEM}(\mathbf{x}_0) = \frac{\mathbf{s}_0^T \hat{\mathbf{R}}^{-1} \mathbf{x}_0}{\mathbf{s}_0^T \hat{\mathbf{R}}^{-1} \mathbf{s}_0}, \quad (4)$$

$$D_{ACE}(\mathbf{x}) = \frac{(\mathbf{s}^T \mathbf{C}^{-1} \mathbf{x})^2}{(\mathbf{s}^T \hat{\mathbf{C}}^{-1} \mathbf{s})(\mathbf{x}^T \hat{\mathbf{C}}^{-1} \mathbf{x})}, \quad (5)$$

$$D_{AMF}(\mathbf{x}) = \frac{(\mathbf{s}^T \hat{\mathbf{C}}^{-1} \mathbf{x})^2}{N \mathbf{s}^T \hat{\mathbf{C}}^{-1} \mathbf{s}}, \quad (6)$$

$$D_{SAM}(\mathbf{x}_0) = \arccos \frac{\mathbf{x}_0^T \mathbf{s}_0}{\|\mathbf{x}_0\| \|\mathbf{s}_0\|}, \quad (7)$$

where  $\hat{\mathbf{R}} = \frac{1}{MN} \sum_{i=1}^M \sum_{j=1}^N \mathbf{x}_0(i, j) \mathbf{x}_0^T(i, j)$  is the estimated correlation matrix and  $\hat{\mathbf{C}} = \frac{1}{MN} \sum_{i=1}^M \sum_{j=1}^N \mathbf{x}(i, j) \mathbf{x}^T(i, j)$  is the estimated covariance matrix. For the compared sparse representation algorithm, we use the classical greedy algorithm orthogonal matching pursuit (OMP) [39] to solve the model proposed in [16] (See equation (20) in [16]). For more details about this sparse representation algorithm, the reader can see [16] for reference. Those 15 kinds of spectra used to simulate the synthetic image 1 are chosen from the U.S. Geological Survey (USGS) Digital Spectral Library [40]. Thus, we can use the USGS Digital Spectral Library as an appropriate spectral library for the sparse representation algorithm. In addition, since we know the exact number of the endmember of synthetic image 1, we can set an appropriate sparsity level, which is an important parameter, for the greedy algorithm. However, for the other experiments, it is hard to construct an appropriate spectral library and set an appropriate sparsity level, so we only compare with the sparse representation algorithm in the synthetic hyperspectral image experiment 1.

Receiver operating characteristic (ROC) [1], [16] curves are used to evaluate the detection results. By taking different thresholds, the ROC curve can plot the varying relationship between the false alarm rate ( $Fa$ ) and the probability of detection ( $Pd$ ), thus the ROC curve can be used to evaluate detection algorithms independently of the threshold selection [1]. The definitions of  $Fa$  and  $Pd$  are [16]:

$$Fa = \frac{N_f}{N}, \quad Pd = \frac{N_c}{N_t}, \quad (8)$$

where  $N_f$  is the number of false alarm pixels;  $N_c$  is the number of correct detection target pixels;  $N$  is the total number of pixels in the hyperspectral image;  $N_t$  is the total number of true target pixels. One can evaluate algorithms from ROC curves. If an algorithm has a higher  $Pd$  under the same  $Fa$  or a lower  $Fa$  under the same  $Pd$  than the other algorithm, the algorithm performs better than the other algorithm.

#### A. Synthetic Hyperspectral Image Experiment 1

The generation process of the synthetic data set used here is the same as that in [20]. 15 kinds of spectra are chosen from the USGS Digital Spectral Library [40] as the endmembers of the synthetic hyperspectral image. These 15 kinds of spectra include: Axinite HS342.3B, Rhodochrosite HS67, Chrysocolla HS297.3B, Niter GDS43 (K-Saltpeper), Anthophyllite HS286.3B, Neodymium Oxide GDS34, Monazite HS255.3B, Samarium Oxide GDS36, Pigeonite HS199.3B, Meionite WS700.HLsep, Spodumene HS210.3B, Labradorite HS17.3B, Grossular WS484, Zoisite HS347.3B and Wollastonite HS348.3B. These spectra have 224 bands with spectral range 0.4-2.5  $\mu\text{m}$ . The generation process for the synthetic data set is as follow [20].

- 1) Set the size of the image scene to  $s^2 \times s^2$  ( $s = 8$ ). Divide the scene into  $s \times s$  regions. Initialize each region with one endmember which is randomly selected from the 15 kinds of endmembers. These 15 kinds of endmembers can form a  $L \times P$  dimension signatures matrix  $\mathbf{W}$  ( $L = 224$ ,  $P = 15$ ).

- 2) Use a simple  $(s + 1) \times (s + 1)$  mean filter to generate mixed pixels. I.e., for a pixel, calculate the mean of its  $(s + 1) \times (s + 1) - 1$  neighboring pixels and use the mean to replace the value of this pixel.
- 3) In order to further remove pure pixels, if in a pixel, the abundance of a single endmember is larger than 70%, replace this pixel with a mixture made up of two endmembers, and set both of the abundances of these two endmembers to 50%. The two endmembers chosen to substitute the original endmembers are the original endmember that has an abundance larger than 70% and its next endmember. For example, if in a pixel, the 1st endmember has an abundance larger than 70%, replace the pixel with a mixture made up of the 1st endmember and the 2nd endmember. If in a pixel, the 15th endmember has an abundance larger than 70%, replace the pixel with a mixture made up of the 15th endmember and the 1st endmember. Now, we have the abundance values of all endmembers for every pixel. Store all the abundance values in a  $P \times K$  ( $K = s^2 \times s^2$ ) dimension matrix  $\mathbf{H}$ .
- 4) Utilize linear spectral mixing model [41] to generate the hyperspectral data:  $\mathbf{Y} = \mathbf{W} \times \mathbf{H}$ .
- 5) Add Gaussian white noise with 30 dB SNR to  $\mathbf{Y}$ .

This synthetic data set is used to detect the Axinite HS342.3B target as an example. Fig. 1(a) and (b) show the first band of the synthetic hyperspectral image and the ground truth of the Axinite HS342.3B target, respectively. The endmember of Axinite HS342.3B is used as the prior spectral signature of target for all algorithms. For the compared sparse representation algorithm, the USGS Digital Spectral Library which contains 498 spectra is used as the spectral library. Since there are 15 endmembers in this synthetic image, we set the sparsity level to 15 for OMP. The detection outputs of different algorithms are shown in Fig. 2. To show the output values in image form, the output values have been normalized to  $[0, 1]$  in Fig. 2. From Fig. 2, we can see that the proposed TVHTD algorithm keeps the spatial homogeneity better than the other algorithms. Fig. 3 shows ROC curves of different algorithms. For this synthetic data set, ROC curves of ACE and AMF are nearly overlapped. ROC curves indicate that TVHTD obtains better results than the other algorithms. Both ACE and AMF are based on hypothesis testing and assume that the target and the background follow particular probability distributions. SAM measures the spectral angle between the spectrum of the test pixel and the prior spectral signature of target. If the hyperspectral image follows probability distributions assumed by ACE or AMF, ACE or AMF can obtain good results. If the spectral angle between the spectrum of the target pixel and the prior spectral signature of target is smaller than that between the spectrum of the background pixel and the prior spectral signature of target, SAM can obtain good results. However, the situation of the real hyperspectral image is very likely to be different, and this may be the reason why ACE, AMF and SAM do not obtain good results in this experiment. The compared sparse representation algorithm also uses a spatial constraint which forces the vector Laplacian of the reconstructed test pixel to equal zero. This constraint is very strong, and this may be the reason why the compared sparse representation algorithm does not obtain the best result. CEM aims to suppress the output of the background. But from Fig. 2, we can see that TVHTD can suppress the output of the background better than CEM. This is because the smoothness property of TV can help in suppressing background. In addition, for this synthetic data set, both the target and the background have the

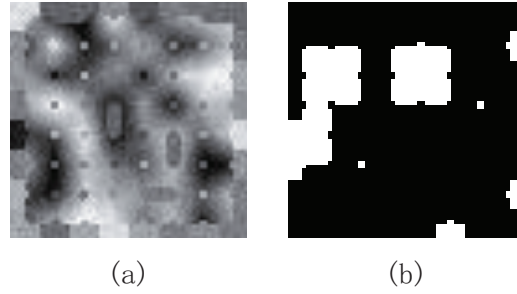


Fig. 1. (a) The first band of the synthetic hyperspectral image 1. (b) The ground truth of the synthetic hyperspectral image 1.

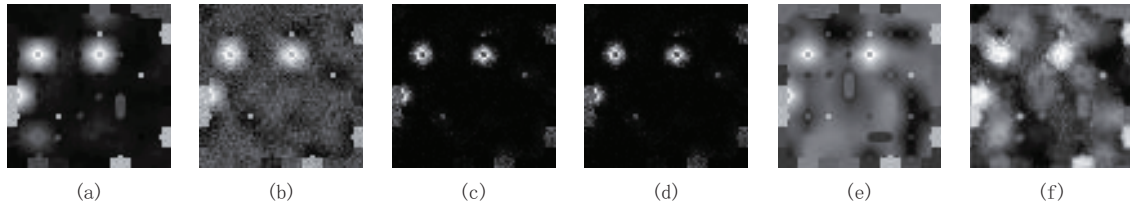


Fig. 2. The detection outputs for the synthetic hyperspectral image 1: (a) TVHTD, (b) CEM, (c) ACE, (d) AMF, (e) SAM and (f) sparse representation algorithm. The output values have been normalized to  $[0, 1]$ .

spatial homogeneity property which can be kept by TV. Fig. 2 shows that in the respect of suppressing background and keeping spatial homogeneity simultaneously, our algorithm performs best. Thus our algorithm obtains better result than the other algorithms.

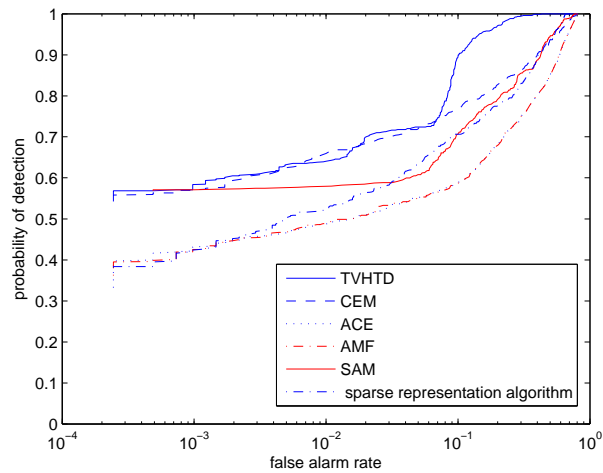


Fig. 3. ROC curves of different algorithms for the synthetic hyperspectral image 1.

### B. Synthetic Hyperspectral Image Experiment 2

We use the method which is similar to that in [42] to design another synthetic hyperspectral image. From a real AVIRIS hyperspectral image which was captured from San Diego airport, San Diego, USA, we chose the spectra from 5 pure pixels: airplane (A), roof (R), grass (G), parking apron (P) and ground (Gd). We also calculate the mean of the real hyperspectral image, and denote it by M. The low SNR and water absorption bands of A, G, R, P, Gd and M are removed, then 189 bands with spectral range 0.4-2.5  $\mu\text{m}$  are left. We normalize the spectra of A, G, R, P, Gd and M to [0, 1] and use these 6 spectra to design a synthetic hyperspectral image with  $200 \times 200$  pixels. Fig. 4 (a) shows the first band of this synthetic hyperspectral image. A is used to simulate targets, and G, R, P, Gd, and M are used to simulate the background. 9 scattered targets with different mixtures between the target endmember and the background endmember are simulated. The ground truth of the 9 scattered targets is shown in Fig. 4 (b). The 9 targets all occupy only one pixel. The locations of 9 targets and the corresponding abundances of the target endmember and background endmembers are shown in Table I. Based on the linear spectral mixing model, the background are generated as follows: for each background pixel, the abundances of R, G, P, Gd and M are generated randomly, and the abundances satisfy the nonnegativity constraint [20] and the sum-to-one constraint [20]. Finally, additive Gaussian white noise is added to the synthetic image to achieve a 20 dB SNR.

In this synthetic image, targets scattering in the background are detected. The spectra of target pixels are not identical. From Table I, we can see that both full pixel targets and sub-pixel targets exist, and the abundances of the target endmember and background endmembers are not same among different target pixels. The spectrum of A is used as the prior spectral signature of target for all algorithms. In this experiment, the targets all occupy only one pixel. Although targets do not have spatial information, backgrounds still have spatial information. The neighbors of background pixels are very likely to be background pixels. TVHTD which minimizes the total variation of the output can keep this spatial homogeneity of background. At the same time, the constraint used in TVHTD can guarantee the target spectra unsuppressed in the output, so targets and backgrounds can be separated effectively in the output. Fig. 5 shows the outputs of different algorithms. In Fig. 5, the output values have been normalized to [0, 1]. ROC curves of different algorithms are shown in Fig. 6. The experiment results demonstrate that in the case of scattering targets with different mixtures between the target endmember and the background endmember, TVHTD can also obtain good result. The ROC curves show that even when the targets all occupy only one pixel, TVHTD can still obtain better results than the other algorithms. Because in such case, the background is kept smooth, and this smoothness can help in suppressing the background, but at the same time the algorithm allows for sharp edges in the detection output.

### C. Real Hyperspectral Image Experiment 1

We use a real Cuprite hyperspectral image [43] collected by AVIRIS to do experiments. The original image has 224 bands with spectral range 0.4-2.5  $\mu\text{m}$ . For the experiment data, the low SNR and water absorption bands have been removed, and 188 bands are left. The size of the experiment image is  $250 \times 191$  pixels. The first band of the Cuprite hyperspectral image is shown in Fig. 7(a). We use this data set to detect the buddingtonite target. The

TABLE I  
THE LOCATIONS OF 9 TARGETS AND THE CORRESPONDING ABUNDANCES OF THE TARGET ENDMEMBER AND BACKGROUND ENDMEMBERS  
IN THE SYNTHETIC HYPERSPECTRAL IMAGE 2

location	(31, 31)	(66, 31)	(101, 31)	(101, 66)	(101, 101)
abundances	A	A	$0.75A + 0.25M$	$0.75A + 0.25R$	$0.75A + 0.25G$
location	(101, 136)	(101, 171)	(136, 31)	(171, 31)	
abundances	$0.75A + 0.25P$	$0.75A + 0.25G$	$0.5A + 0.5M$	$0.25A + 0.75M$	

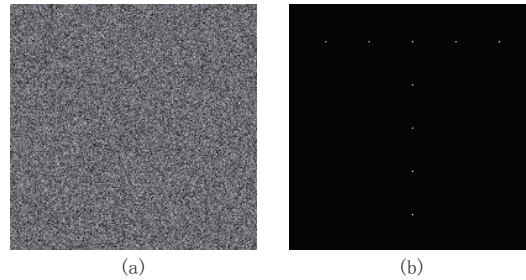


Fig. 4. (a) The first band of the synthetic hyperspectral image 2. (b) The ground truth of the synthetic hyperspectral image 2.

ground truth [44] of the buddingtonite target is shown in Fig. 7(b). The mean of two buddingtonite spectra in the USGS Digital Spectral Library [40] is used as the prior spectral signature of target for all algorithms. The detection outputs of different algorithms are shown in Fig. 8. The output values have been normalized to  $[0, 1]$  in Fig. 8. ROC curves of different algorithms are shown in Fig. 9. Fig. 9 shows that our algorithm outperforms the other algorithms in this experiment.

#### D. Real Hyperspectral Image Experiment 2

Here, we use the HyMap data set obtained from the Rochester Institute of Technology Hyperspectral Target Detection Blind Test website [45], [46] to do experiments. The self test set in spectral reflectance provided by the website is used. The size of the HyMap image is  $280 \times 800$  pixels, and the spectral range is  $0.45\text{-}2.5 \mu\text{m}$  with 126 bands. We remove the low SNR as well as water absorption bands, and use 124 bands in the experiment. The

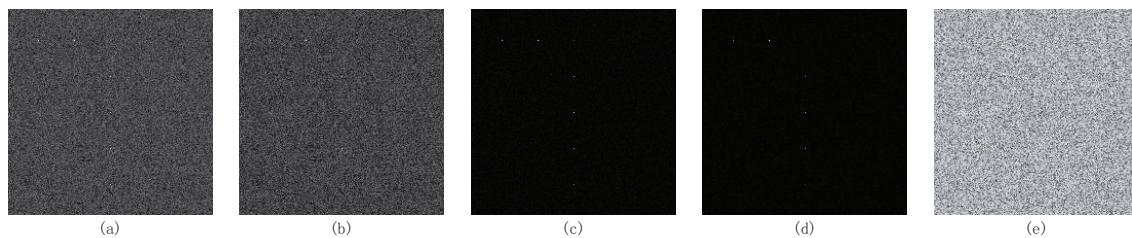


Fig. 5. The detection outputs for the synthetic hyperspectral image 2: (a) TVHTD, (b) CEM, (c) ACE, (d) AMF and (e) SAM. The output values have been normalized to  $[0, 1]$ .

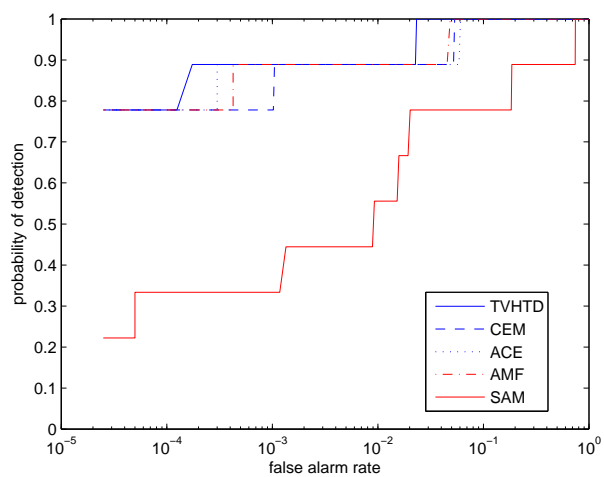


Fig. 6. ROC curves of different algorithms for the synthetic hyperspectral image 2.

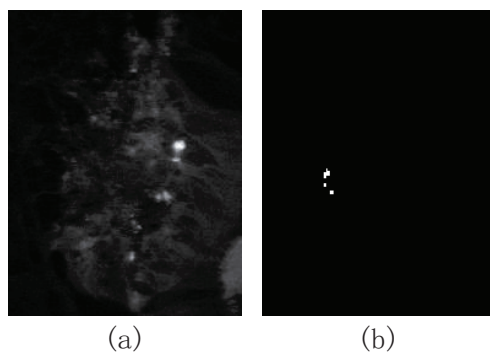


Fig. 7. (a) The first band of the Cuprite hyperspectral image. (b) The ground truth of the buddingtonite target.

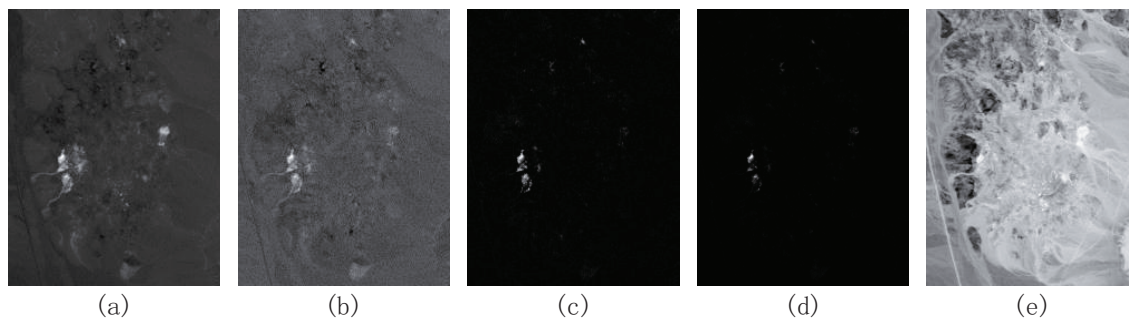


Fig. 8. The detection outputs for the Cuprite hyperspectral image: (a) TVHTD, (b) CEM, (c) ACE, (d) AMF and (e) SAM. The output values have been normalized to  $[0, 1]$ .

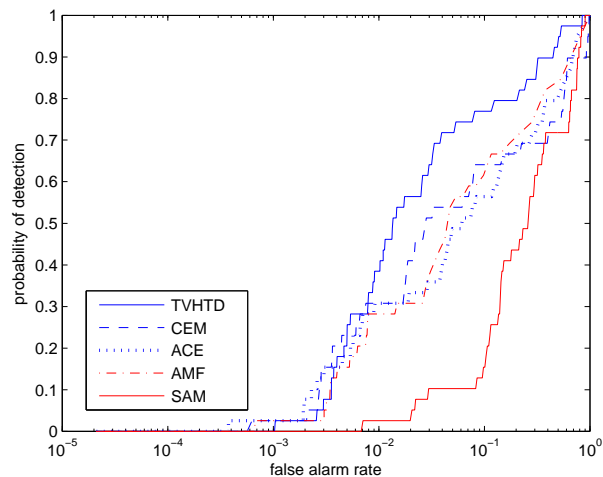


Fig. 9. ROC curves of different algorithms for the Cuprite hyperspectral image.

first band of the HyMap self test set is shown in Fig. 10(a). There are three vehicle targets called V1, V2 and V3, respectively. We use the self test set to detect all these three vehicle targets. The spectral signatures of targets and ground truths are also obtained from the website. V1, V2 and V3 all occupy only one pixel. Fig. 10(b) shows the locations of V1, V2 and V3 in the HyMap self test set (ground truths of V1, V2 and V3). The reflectance data set provided by the website is scaled by 10000. In the experiment, we use the unscaled data by dividing the original reflectance data by 10000. To make the magnitudes of spectral signatures of targets similar to the HyMap data set and make the magnitudes in the range of  $[0, 1]$ , we divide the spectral signatures of targets provided by the website by 100. Two different spectral signatures are provided by the website for V2. We use the white truck's paint one.

The detection outputs for V1 are shown in Fig. 11. In Fig. 11, the output values have been normalized to  $[0, 1]$ . From Fig. 11, we can see that TVHTD can keep the spatial smoothness or homogeneity of output values. The output of AMF seems to have spatial smoothness or homogeneity too. However, this may be because the output values of most pixels of AMF are small which can be seen in Fig. 11. Since V1, V2 and V3 all occupy only one pixel, it is not suitable to evaluate algorithms using ROC curves. A score that the number of pixels which have equal or larger outputs than the output of the target location pixel can be given to a detection result [45]. Obviously, the smaller the score is, the better the detection result is, and a perfect score is 1 which means the target location pixel has the largest output [45]. The scores of different algorithms are shown in Table II. The last row of Table II shows the mean scores of V1, V2 and V3. The bold ones denote the best results. It can be seen from Table II that for V1 and V3, TVHTD has the best results. For V2, SAM has better result than TVHTD. This may be because the spectrum of V2 location pixel has small spectral angle with the prior spectral signature of V2. However, for other real hyperspectral images, the spectral angles between background spectra and the prior spectral signature of target are even smaller than those between target spectra and the prior spectral signature of target. In such case, SAM which only measures the spectral angle between the spectrum of the test pixel and the prior spectral signature

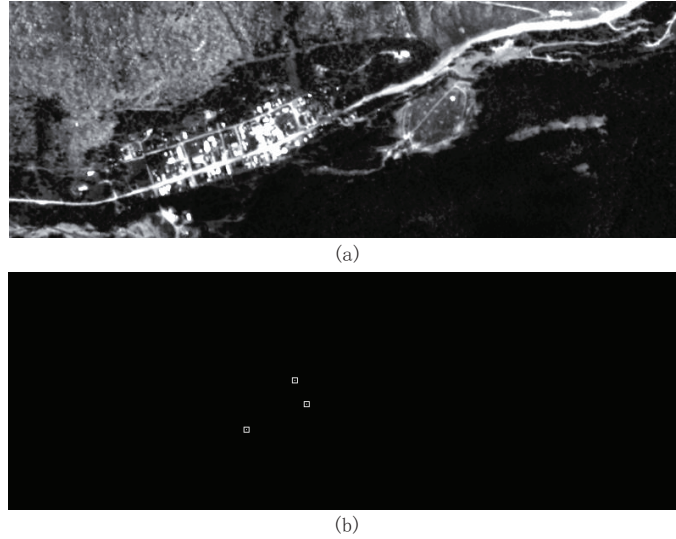


Fig. 10. (a) The first band of the HyMap self test set. (b) The ground truths of V1, V2 and V3 for the HyMap self test set. The bright point in the middle square is the location of V1, and the bright point in the right square is the location of V2, and the bright point in the left square is the location of V3.

of target can not obtain good results. This can be demonstrated from that SAM only obtains good result for V2, and for V1 and V3, SAM has very poor detection results. In fact, no one algorithm has the best results for all the targets. The mean scores also show that our algorithm obtains much better result than the other algorithms. Thus, we can conclude that for the HyMap self test set, overall our algorithm outperforms the other algorithms.

In this experiment, similar to the synthetic image 2, the targets all occupy only one pixel. In such case, TVHTD still obtains better results than the other algorithms. The experiment results once again demonstrate that even when the target occupies only one pixel, TVHTD can still get satisfactory results. Because in such case, the background is kept smooth, but at the same time the algorithm allows for sharp edges in the detection output. In addition, keeping the background smooth can help in suppressing the background, and at the same time the constraint used in TVHTD can guarantee the target spectra unsuppressed in the output.

TABLE II  
THE SCORES OF DIFFERENT ALGORITHMS FOR THE HYMAP SELF TEST SET

target	TVHTD	CEM	ACE	AMF	SAM
V1	<b>2486</b>	4415	7970	8225	8252
V2	3759	55372	111212	97822	<b>2278</b>
V3	<b>2812</b>	2862	4061	4343	20747
mean	<b>3019</b>	20883	41081	36797	10426

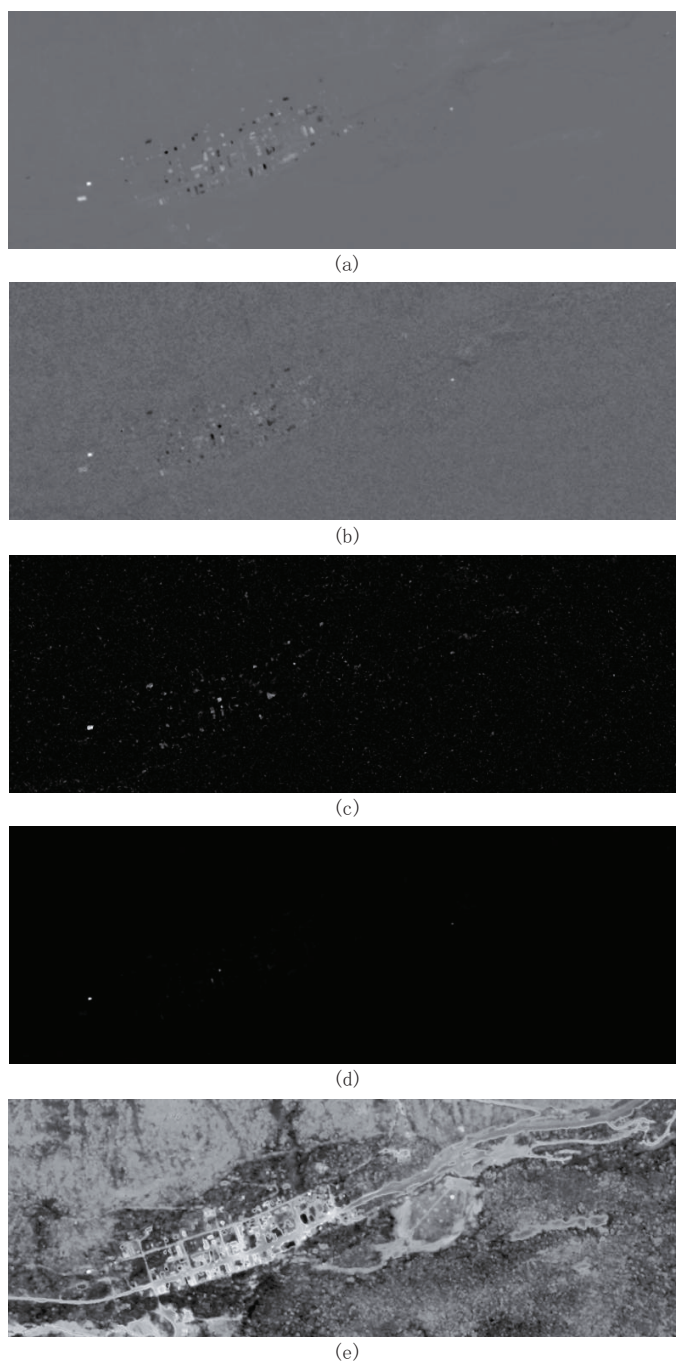


Fig. 11. The detection outputs of V1 for the HyMap self test set: (a) TVHTD, (b) CEM, (c) ACE, (d) AMF and (e) SAM. The output values have been normalized to  $[0, 1]$ .

### E. Computational Complexity and Execution Time Analyses

Next, we give the computational complexity analyses of Algorithm 1. The complexities of calculating  $\beta\mathbf{ss}^T + \lambda\mathbf{HH}^T + \lambda\mathbf{VV}^T$  and  $\beta f^k \mathbf{s} + \lambda \mathbf{H} \mathbf{d}_x^k - \lambda \mathbf{H} \mathbf{b}_x^k + \lambda \mathbf{V} \mathbf{d}_y^k - \lambda \mathbf{V} \mathbf{b}_y^k$  are  $O(MNL^2)$  and  $O(MNL)$ , respectively. When obtain the value of  $\beta\mathbf{ss}^T + \lambda\mathbf{HH}^T + \lambda\mathbf{VV}^T$ , the complexity of  $(\beta\mathbf{ss}^T + \lambda\mathbf{HH}^T + \lambda\mathbf{VV}^T)^{-1}$  is  $O(L^3)$ . Thus the complexity of step 4 is  $O(\max\{MNL^2, L^3\})$ . The complexities of step 5, step 6, step 7 and step 8 are all  $O(MNL)$ . So, the complexity of the "for" loop is  $O(\max\{MNL^2, L^3\})$ . The complexity of step 10 is  $O(L)$ . Finally, the total complexity for Algorithm 1 is  $O(\max\{MNL^2, L^3\})$ .

The execution times of different algorithms for synthetic hyperspectral image 1 are given in Table III. All algorithms are implemented on MATLAB R2010a on a PC with an Intel Core i5 CPU (2.60 GHz) and a 4 GB RAM. Table III shows the sparse representation algorithm need the most time. Although TVHTD consumes more time than CEM, ACE, AMF and SAM, TVHTD obtains the best result among different algorithms for synthetic hyperspectral image 1.

TABLE III  
THE EXECUTION TIMES OF DIFFERENT ALGORITHMS FOR THE SYNTHETIC HYPERSPECTRAL IMAGE 1

algorithm	TVHTD	CEM	ACE	AMF	SAM	sparse representation algorithm
time (s)	7.6545	0.0354	0.0911	0.0557	0.0233	1578.0169

## V. CONCLUSION

In hyperspectral images, the neighbors of target pixels are very likely to be target pixels and those of background pixels are very likely to be background pixels. In this paper, we propose a novel TV based hyperspectral target detection algorithm to keep this spatial homogeneity in detection output. The target detection problem is transformed to an  $\ell_1$  norm convex optimization problem. The Split Bregman algorithm is utilized to solve the formulated optimization problem efficiently. We use two synthetic hyperspectral images and two real hyperspectral images to conduct experiments, and the experiment results show our algorithm obtains better results than other algorithms.

## ACKNOWLEDGMENT

The authors would like to thank the handling editor and all anonymous reviewers who provided very insightful and helpful comments.

## REFERENCES

- [1] D. Manolakis, D. Marden, and G. A. Shaw, "Hyperspectral image processing for automatic target detection applications," *Lincoln Lab. J.*, vol. 14, no. 1, pp. 79-116, 2003.
- [2] D. Manolakis and G. Shaw., "Detection algorithms for hyperspectral imaging applications," *IEEE Signal Process. Mag.*, vol. 19, no. 1, pp. 29-43, Jan. 2002.
- [3] G. A. Shaw and H. K. Burke, "Spectral imaging for remote sensing," *Lincoln Lab. J.*, vol. 14, no. 1, pp. 3-28, 2003.

- [4] F. A. Kruse, "The Spectral Image Processing System (SIPS)-Interactive visualization and analysis of imaging spectrometer data," *Remote Sens. Environ.*, vol. 44, no. 2/3, pp. 145-163, May/June. 1993.
- [5] W. H. Farrand and J. C. Harsanyi, "Mapping the distribution of mine tailings in the Couer d'Alene River valley, Idaho, through the use of a constrained energy minimization technique," *Remote Sens. Environ.*, vol. 59, no. 1, pp. 64-76, Jan. 1997.
- [6] J. C. Harsanyi, Detection and classification of subpixel spectral signatures in hyperspectral image sequences, Ph.D. dissertation, University of Maryland Baltimore County, 1993.
- [7] D. Manolakis, R. Lockwood, T. Cooley, and J. Jacobson, "Is there a best hyperspectral detection algorithm?" in *Proc SPIE*, Orlando, USA, 2009.
- [8] S. Kraut and L. L. Scharf, "The CFAR adaptive subspace detector is a scale-invariant GLRT," *IEEE Trans. Signal Process.*, vol. 47, no. 9, pp. 2538-2541, Sept. 1999.
- [9] S. Kraut, L. L. Scharf, and L. T. McWhorter, "Adaptive subspace detectors," *IEEE Trans. Signal Process.*, vol. 49, no. 1, pp. 1-16, Jan. 2001.
- [10] F. C. Robey, D. R. Fuhrmann, E. J. Kelly, and R. Nitzberg, A CFAR adaptive matched filter detector, *IEEE Trans. Aerosp. Electron. Syst.*, vol. 28, no. 1, pp. 208-218, Jan. 1992.
- [11] W.-S. Chen and I. S. Reed, A new CFAR detection test for radar, *Digital Signal Process.*, vol. 1, no. 4, pp. 198-214, Oct. 1991.
- [12] J. C. Harsanyi and C.-I. Chang, "Hyperspectral image classification and dimensionality reduction: An orthogonal subspace projection approach," *IEEE Trans. Geosci. Remote Sens.*, vol. 32, no. 4, pp. 779-785, Jul. 1994.
- [13] S. M. Kay, *Fundamentals of Statistical Signal Processing*. Englewood Cliffs, NJ: Prentice Hall, 1998.
- [14] L. L. Scharf and B. Friedlander, "Matched subspace detectors," *IEEE Trans. Signal Process.*, vol. 42, no. 8, pp. 2146-2156, Aug. 1994.
- [15] Q. Du, H. Ren, and C.-I. Chang, "A comparative study for orthogonal subspace projection and constrained energy minimization," *IEEE Trans. Geosci. Remote Sens.*, vol. 41, no. 6, pp. 1525-1529, Jun. 2003.
- [16] Y. Chen, N. M. Nasrabadi, and T. D. Tran, "Sparse representation for target detection in hyperspectral imagery," *IEEE J. Sel. Top. Sign. Proces.*, vol. 5, no. 3, pp. 629-640, Jun. 2011.
- [17] Y. Chen, N. M. Nasrabadi, and T. D. Tran, "Simultaneous joint sparsity model for target detection in hyperspectral imagery," *IEEE Geosci. Remote Sens. Lett.*, vol. 8, no. 4, pp. 676-680, Jul. 2011.
- [18] Z. Huang, Z. Shi, and S. Yang, "Nonlocal similarity regularized sparsity model for hyperspectral target detection," *IEEE Geosci. Remote Sens. Lett.*, vol. 10, no. 6, pp. 1532-1536, Nov. 2013.
- [19] A. M. Bruckstein, D. L. Donoho and M. Elad, From sparse solutions of systems of equations to sparse modeling of signals and images, *Siam Rev.*, vol. 51, no. 1, pp. 34-81, 2009.
- [20] Z. Shi, W. Tang, Z. Duren, and Z. Jiang, "Subspace matching pursuit for sparse unmixing of hyperspectral data," *IEEE Trans. Geosci. Remote Sens.*, vol. 52, no. 6, pp. 3256-3274, Jun. 2014.
- [21] H. Kwon and N. M. Nasrabadi, "Kernel matched subspace detectors for hyperspectral target detection," *IEEE Trans. Pattern Anal. Mach. Intell.*, vol. 28, no. 2, pp. 178-194, Feb. 2006.
- [22] H. Kwon and N. M. Nasrabadi, "Kernel adaptive subspace detector for hyperspectral imagery," *IEEE Geosci. Remote Sens. Lett.*, vol. 3, no. 2, pp. 271-275, Apr. 2006.
- [23] L. Zhang, L. Zhang, D. Tao, and X. Huang, "Sparse transfer manifold embedding for hyperspectral target detection," *IEEE Trans. Geosci. Remote Sens.*, vol. 52, no. 2, pp. 1030-1043, Feb. 2014.
- [24] L. Zhang, L. Zhang, D. Tao, X. Huang and B. Du, "Hyperspectral remote sensing image subpixel target detection based on supervised metric learning," *IEEE Trans. Geosci. Remote Sens.*, vol. 52, no. 8, pp. 4955-4965, Aug. 2014.
- [25] Y. Dong, B. Du, and L. Zhang, "Target detection based on random forest metric learning," *IEEE J. Sel. Top. Appl. Earth Obs. Remote Sens.*, vol. 8, no. 4, pp. 1830-1838, Apr. 2015.
- [26] L. Rudin, S. Osher, and E. Fatemi, "Nonlinear total variation based noise removal algorithms," *Phys. D, Nonlinear Phenom.*, vol. 60, no. 1-4, pp. 259-268, Nov. 1992.
- [27] Z. Guo, T. Wittman, and S. Osher, "L1 unmixing and its application to hyperspectral image enhancement," in *Proc. SPIE Conf. Algorithms Technol. Multispectr., Hyperspectr., Ultraspectr. Imagery XV*, Orlando, FL, 2009, vol. 7334, pp. 73 341-73 449.
- [28] A. Chambolle, "An algorithm for total variation minimization and applications," *J. Math. Imag. Vis.*, vol. 20, no. 1/2, pp. 89-97, Jan.-Mar. 2004.

- [29] M.-D. Iordache, J. M. Bioucas-Dias, and A. Plaza, "Total variation spatial regularization for sparse hyperspectral unmixing," *IEEE Trans. Geosci. Remote Sens.*, vol. 50, no. 11, pp. 4484-4502, Nov. 2012.
- [30] S. Osher, M. Burger, D. Goldfarb, J. Xu, and W. Yin, "An iterative regularization method for total variation-based image restoration," *Multiscale Model. Simul.*, vol. 4, no. 2, pp. 460-489, 2005.
- [31] T. Goldstein and S. Osher, "The split Bregman method for L1-regularized problems," *SIAM J. Imaging Sci.*, vol. 2, no. 2, pp. 323-343, 2009.
- [32] Z. Shi, Z. Qin, S. Yang, and Z. Jiang, "Spatial multiple materials detection in hyperspectral imagery," in *Proc. Int. Conf. Aware. Sci. Technol., iCAST*, Dalian, China, 2011, pp. 76-80.
- [33] A. Ifarraguerri and C.-I. Chang, "Unsupervised hyperspectral image analysis with projection pursuit," *IEEE Trans. Geosci. Remote Sens.*, vol. 38, no. 6, pp. 2529-2538, Nov. 2000.
- [34] S.-S. Chiang, C.-I. Chang, and I. W. Ginsberg, "Unsupervised target detection in hyperspectral images using projection pursuit," *IEEE Trans. Geosci. Remote Sens.*, vol. 39, no. 7, pp. 1380-1391, Jul. 2001.
- [35] L. M. Bregman, "The relaxation method of finding the common points of convex sets and its application to the solution of problems in convex optimization," *USSR Comput. Math. and Math. Phys.*, vol. 7, no. 3, pp. 200-217, 1967.
- [36] J. Xu and S. Osher, "Iterative regularization and nonlinear inverse scale space applied to wavelet-based denoising," *IEEE Trans. Image Process.*, vol. 16, no. 2, pp. 534-544, Feb. 2007.
- [37] Z. Shi, Z. An, and Z. Jiang, "Hyperspectral image fusion by the similarity measure-based variational method," *Opt. Eng.*, vol. 50, no. 7, 077006, Jul. 2011.
- [38] P. L. Combettes and J.-C. Pesquet, "Proximal splitting methods in signal processing," in: *Fixed-Point Algorithms for Inverse Problems in Science and Engineering*, (H. H. Bauschke, R. S. Burachik, P. L. Combettes, V. Elser, D. R. Luke, and H. Wolkowicz, Editors), pp. 185-212. Springer, New York, 2011.
- [39] J. A. Tropp, "Signal Recovery From Random Measurements Via Orthogonal Matching Pursuit," *IEEE Trans. Inf. Theory*, vol. 53, no. 12, pp. 4655-4666, Dec. 2007.
- [40] R. N. Clark, G. A. Swayze, A. J. Gallagher, T. V. V. King, and W. M. Calvin, "The U.S. geological survey digital spectral library: Version 1: 0.2 to 3.0 microns," U.S. Geol. Survey, Denver, CO, USA, Open File Rep., pp. 93-592, 1993.
- [41] J. B. Adams, M. O. Smith, and A. R. Gillespie, *Remote Geochemical Analysis: Elemental and Mineralogical Composition*. Cambridge, U.K.: Cambridge Univ. Press, 1993.
- [42] Y.-C. C. Chang, H. Ren, C.-I. Chang, and R. S. Rand, How to design synthetic images to validate and evaluate hyperspectral imaging algorithms, in *Proc. SPIE Int. Soc. Opt. Eng.M*, Orlando, FL, USA, 2008, p. 69661P.
- [43] AVIRIS Cuprite data set. [Online]. Available: <http://aviris.jpl.nasa.gov/html/aviris.freedata.html>
- [44] USGS map of the distribution of different minerals in the Cuprite mining district in Nevada. [Online]. Available: <http://speclab.cr.usgs.gov/PAPERS/tetracorder/>
- [45] D. Snyder *et al.*, "Development of a web-based application to evaluate target finding algorithms," in *Proc. IEEE Int. Geosci. Remote Sens. Symp.*, Boston, MA, USA, 2008, pp. II915-II918.
- [46] J. Kerekes and D. Snyder. Target Detection Blind Test. [Online]. Available: <http://dirsapps.cis.rit.edu/blindtest/>



**Shuo Yang** received the B.Eng. degree in electronic information science and technology from the Shandong University, Weihai, China, in 2009, and received the Ph.D. degree in pattern recognition and intelligent system from the Image Processing Center, School of Astronautics, Beihang University, Beijing, China, in 2016.

His research interests include hyperspectral image target detection, image processing, and pattern recognition.



**Zhenwei Shi** (M13) received his Ph.D. degree in mathematics from Dalian University of Technology, Dalian, China, in 2005. He was a Postdoctoral Researcher in the Department of Automation, Tsinghua University, Beijing, China, from 2005 to 2007. He was Visiting Scholar in the Department of Electrical Engineering and Computer Science, Northwestern University, U.S.A., from 2013 to 2014. He is currently a professor and the chairman of the Image Processing Center, School of Astronautics, Beihang University. His current research interests include remote sensing image processing and analysis, computer vision, pattern recognition, and machine learning.

He has authored or co-authored over 100 scientific papers in refereed journals and proceedings, including the IEEE Transactions on Pattern Analysis and Machine Intelligence, the IEEE Transactions on Neural Networks, the IEEE Transactions on Geoscience and Remote Sensing, the IEEE Geoscience and Remote Sensing Letters and the IEEE Conference on Computer Vision and Pattern Recognition.